

NIGHTSIDE WINDS AT THE LOWER CLOUDS OF VENUS WITH AKATSUKI/IR2: LONGITUDINAL, LOCAL TIME AND DECADAL VARIATIONS FROM COMPARISON WITH PREVIOUS MEASUREMENTS.

JAVIER PERALTA,¹ KEISHIRO MUTO,² RICARDO HUESO,³ TAKESHI HORINOCHI,⁴ AGUSTÍN SÁNCHEZ-LAVEGA,³ SHIN-YA MURAKAMI,¹ PEDRO MACHADO,⁵ ELIOT F. YOUNG,⁶ YEON JOO LEE,² TORU KOUYAMA,⁷ HIDEO SAGAWA,⁸ KEVIN MCGOULDRIK,⁹ TAKEHIKO SATOH,^{1,10} TAKESHI IMAMURA,² SANJAY S. LIMAYE,¹¹ TAKAO M. SATO,^{12,1} KAZUNORI OGOHARA,¹³ MASATO NAKAMURA,¹ AND DAVID LUZ⁵

¹*Institute of Space and Astronautical Science (ISAS), Japan Aerospace Exploration Agency (JAXA) 3-1-1, Yoshinodai, Chuo-ku, Sagami-hara, Kanagawa, 252-5210, Japan*

²*Graduate School of Frontier Sciences, The University of Tokyo, Japan*

³*Escuela de Ingeniería de Bilbao (UPV/EHU), Bilbao, Spain*

⁴*Faculty of Environmental Earth Science, Hokkaido University, Sapporo, Japan*

⁵*Institute of Astrophysics and Space Sciences, Portugal*

⁶*Southwest Research Institute, Boulder, CO 80302, USA*

⁷*Artificial Intelligence Research Center, National Institute of Advanced Industrial Science and Technology, Tokyo, Japan*

⁸*Faculty of Science, Kyoto Sangyo University, Japan*

⁹*Laboratory for Atmospheric and Space Physics, University of Colorado Boulder, Boulder, CO 80303-7814, USA*

¹⁰*Department of Space and Astronautical Science, School of Physical Sciences, Sokendai, Japan*

¹¹*Space Science and Engineering Center, University of Wisconsin-Madison, Madison, USA*

¹²*Space Information Center, Hokkaido Information University, Hokkaido, Japan*

¹³*School of Engineering, University of Shiga Prefecture, Shiga, Japan*

(Dated: Published in *Astrophysical Journal Supplement Series* the 7 of December 2018; original manuscript [here](#).)

ABSTRACT

We present measurements of the wind speeds at the nightside lower clouds of Venus from observations by JAXA's mission Akatsuki during 2016, complemented with new wind measurements from ground-based observations acquired with TNG/NICS in 2012 and IRTF/SpeX in 2015 and 2017. Zonal and meridional components of the winds were measured from cloud tracking on a total of 466 Akatsuki images of Venus acquired by the camera IR2 using the 2.26- μm filter, with spatial resolutions ranging 10–80 km per pixel and covering from 2016 March 22 to October 31. More than 149,000 wind vectors were obtained with an automatic technique of template matching, and 2,947 wind vectors were inferred with the manual procedure. The meridional profiles for both components of the winds are found to be consistent with results from the Venus Express mission during 2006–2008, although stronger wind variability is found for the zonal component at equatorial latitudes where Akatsuki observations have better viewing geometry than Venus Express. The zonal winds at low latitudes also suggest a zonal variability that could be associated with solar tides or vertically propagating orographic waves. Finally, the combination of our wind measurements from TNG/NICS, IRTF/SpeX and Akatsuki images with previously published and based in data from 1978 to 2017 suggests variations of up to 30 m s⁻¹ in the winds at the lower clouds of the Venus nightside.

Keywords: planets and satellites: atmospheres, planets and satellites: terrestrial planets

1. INTRODUCTION

The atmospheric circulation of Venus from the surface up to the stratosphere is dominated by a retrograde zonal superrotation (h.a. RZS) which, according to both *in situ* (Counselman et al. 1980) and cloud tracking measurements (Sánchez-Lavega et al. 2008), attains the

fastest wind speeds at the top of Venus’s cloud layer (Schubert 1983; Gierasch et al. 1997; Sánchez-Lavega et al. 2017). The cloud layer is also where most of the energy from the solar radiation is deposited (Lee et al. 2015b), so a detailed characterization of the atmospheric circulation at multiple levels of the clouds (Sánchez-Lavega et al. 2008; Peralta et al. 2017b) seems essential to properly evaluate the sources and transport of angular momentum in the atmosphere. The wind speeds at the upper clouds of Venus (60–70 km above the surface) are customarily characterized with cloud tracking on both day (Rossow et al. 1990; Belton et al. 1991; Peralta et al. 2007; Limaye 2007; Kouyama et al. 2013; Khatuntsev et al. 2013; Hueso et al. 2015; Horinouchi et al. 2018) and night sides (Peralta et al. 2017c), while the winds at the deeper middle and lower clouds (about 48–60 km) have been evaluated following cloud features visible on the dayside of the planet on the albedo at near infrared wavelengths (Belton et al. 1991; Hueso et al. 2015; Khatuntsev et al. 2017) and in the lower clouds on the nightside (Sánchez-Lavega et al. 2008; Hueso et al. 2012; Horinouchi et al. 2017b) thanks to inhomogeneities in the opacity of the lower clouds which can be observed at the infrared windows at 1.7 and 2.2–2.3 μm (Peralta et al. 2017a).

After the discovery of these infrared spectral windows by Allen & Crawford (1984), and before the arrival of Akatsuki (Nakamura et al. 2016), ESA’s Venus Express mission (h.a. VEx) characterized the RZS at the deeper clouds with unprecedented detail during 2006–2008. However, constraints due to VEx’s polar orbit (Titov et al. 2006) and the long exposure times required by the imaging spectrometer VIRTIS-M (Piccioni et al. 2007) limited observations to the southern hemisphere of Venus with lower quality results at equatorial and lower latitudes (Sánchez-Lavega et al. 2008; Hueso et al. 2012; McGouldrick et al. 2012; Peralta et al. 2017b). As a result, the circulation at the level of the deeper clouds is yet poorly characterized in the northern hemisphere where only sparse measurements exist from ground-based observations (Crisp et al. 1989, 1991; Chanover et al. 1998; Limaye et al. 2006) and images from the Near-Infrared Mapping Spectrometer (NIMS) instrument during the flyby of NASA’s Galileo in 1990 (Carlson et al. 1991). Since its orbit insertion in 2015 December, JAXA’s Akatsuki orbiter has permitted an invaluable opportunity to study this deeper atmospheric circulation on both hemispheres thanks to its equatorial orbit (Nakamura et al. 2016) and the images provided by the 2- μm camera IR2 (Satoh et al. 2016).

In this work we present the first global measurements of the wind speeds at the nocturnal lower clouds of Venus during the first year of Akatsuki observations. A description of the observations performed by the IR2 camera, the processing of the images, navigation corrections and methods of cloud tracking are introduced in section 2. The lower clouds’ morphologies, the meridional profiles of wind speeds and the possible relation between morphologies and speeds are presented in section 3. The wind speeds’ dependence on the size and opacity of the clouds, the local time and an exploration of possible relations with the surface topography is studied in section 4, while the temporal variation of the winds of the lower clouds is presented in section 5. Finally, the main conclusions of this work are presented in section 6.

2. METHODS

After failing its originally-planned orbit insertion in 2010 December 7, Akatsuki orbited the Sun for 5 years and was inserted with success into a Venus orbit in 2015 December (Nakamura et al. 2016). At present, the orbiter performs a westward equatorial orbit with an apoapsis of $\sim 360,000$ km, periapsis ranging 1,000–8,000 km, and a rotation period of about 10 days. Among the payload, the camera IR2 was designed to sense the deep clouds of Venus and infer information about the atmospheric compounds below the cloud layer thanks to its narrow-band filters centered at 1.74, 2.26 and 2.32 μm (Satoh et al. 2016). The scientific objectives of these filters include the study of the morphology of the clouds and their motions, the aerosols’ properties or the abundance of the CO below the clouds (Satoh et al. 2017). Because of the highly eccentric orbit of Akatsuki, the spatial resolution of Venus in the IR2 images varies from 74–12 km per pixel for off-pericenter observations, to 1.6–0.2 km during pericentric ones (Nakamura et al. 2016). Unfortunately, the acquisition of IR2 images was indefinitely interrupted in 2016 December 9 when the electronic device controlling the IR1 and IR2 cameras started to experience an unstable power consumption that has persisted through the present time (Iwagami et al. 2018).

In addition to the IR2 images, new wind measurements have been obtained in this work with ground-based images of Venus acquired after the failure of the infrared channel of the VIRTIS-M (Hueso et al. 2012) instrument on VEx and before and after the time period covered by Akatsuki IR2 observations. The Near Infrared Camera Spectrometer (NICS) (Baffa et al. 2001) at the Ital-

ian National Telescope Galileo (TNG) at La Palma (Canary Islands, Spain) was used to acquire images of the nightside of Venus during 2012 July 11–13 (Mota Machado et al. 2016), while the Medium-Resolution 0.8–5.5 Micron Spectrograph and Imager (SpeX) (Rayner et al. 2003) at the 3-m National Aeronautics and Space Administration Infrared Telescope Facility (IRTF) was used to provide images of Venus with the K-continuum filter in 2015 September and 2017 January–February (Lee et al. 2017a). The wind measurements from these ground-based images will be presented in section 5.

2.1. Image processing

IR2 acquired a total of 1,671 images¹ of the nightside of Venus with the filters 1.74, 2.26 and 2.32 μm (Satoh et al. 2017) among which $\sim 1,370$ were regarded as suitable for cloud tracking. Satoh et al. (2017, fig. 8a therein) reported a problem of light contamination in the IR2 images, consisting of the presence of *halation* rings and a cross pattern extending both horizontally and vertically around the saturated dayside of Venus and spreading with multiple reflections along the PtSi detector. Since this contamination is more reduced in the images taken with the 2.26- μm filter, we restricted our cloud tracking study to this data set composed of 466 images (although additional sets with 1.74- μm images were used in the case of automated cloud tracking). The calibration version of the IR2 images used in this work (“v20170601”) does not include any of the corrections for the light contamination proposed by Satoh et al. (2017) and an alternative image processing technique was applied. This consisted in an adjustment of the brightness/contrast, followed by sharpening the images with an unsharp-mask technique, and finishing with the application of adaptive histogram equalization (see examples in Fig. 1). Images acquired with ground-based instruments at TNG and IRTF also suffered from contamination from the illuminated side of the planet and were processed similarly. Some examples of these images are shown in section 5.

2.2. Navigation of IR2 and ground-based images

Uncertainties such as the thermal distortion affecting the Akatsuki spacecraft and the cameras onboard prevent high accuracy in the navigation of the Venus images at present, so additional corrections in the navigation are yet required (Ogohara et al. 2017; Satoh et al. 2017).

In recently published studies with Akatsuki (Fukuhara et al. 2017; Horinouchi et al. 2017b; Lee et al. 2017b; Horinouchi et al. 2018) the navigation of the images was corrected with an algorithm able to perform an ellipse fitting from an automatic determination of the planetary limb pixels (Ogohara et al. 2012, 2017). This automatized identification of the limb becomes rather uncertain in many of the IR2 nightside images because of the light contamination previously described, and also due to the frequent darkening of the planetary limb because of the strong variability of the clouds’ opacity at lower latitudes McGouldrick et al. (2008); Satoh et al. (2017). Instead, we coded an interactive tool inspired on the software WinJupos (Hahn & Jacquesson 2012) which allows the interactive adjustment of the position, size and orientation of the planet’s grid², using as reference four locations of the limb chosen by the user (see Fig. 2). The visualization of the limb was improved by interactively modifying the brightness and contrast in each image. In the case of the IR2 images, the position of the grid was adjusted with a precision of 1/10th of pixel, its size was increased in some cases (less than 1.3% in all the cases), while the orientation of the grid required no corrections. Regarding the ground-based images from NICS and SpeX, these were navigated using NASA’s SPICE kernels (Acton 1996; Folkner et al. 2009), both the position and orientation of the grid were adjusted, and the predicted size was accurate enough to require no further corrections.

2.3. Techniques for Cloud Tracking

After correcting the navigation and processing the images, these were geometrically projected onto equirectangular (cylindrical) geometry with an angular resolution similar to the best resolution in the original images. In those cases of nightside images acquired when Akatsuki was closer to its pericenter, the better spatial resolution enabled measuring wind speeds at polar latitudes and azimuthal equidistant (polar) projections were performed too using an angular resolution similar to that found at latitudes of about 70° in the original image. Figure 3 shows examples of the original observations, their navigation after corrections and cylindrical and polar maps. For the measurement of wind speeds, two different techniques of cloud tracking were employed: (a) a *manual method* applied to the full data set of IR2 and ground-based images (see Table 1), consisting of a manual search of the cloud tracer followed by a fine ad-

¹ Available at: <http://darts.isas.jaxa.jp/planet/project/akatsuki/>

² The corrected geometry files are available from the corresponding author on reasonable request.

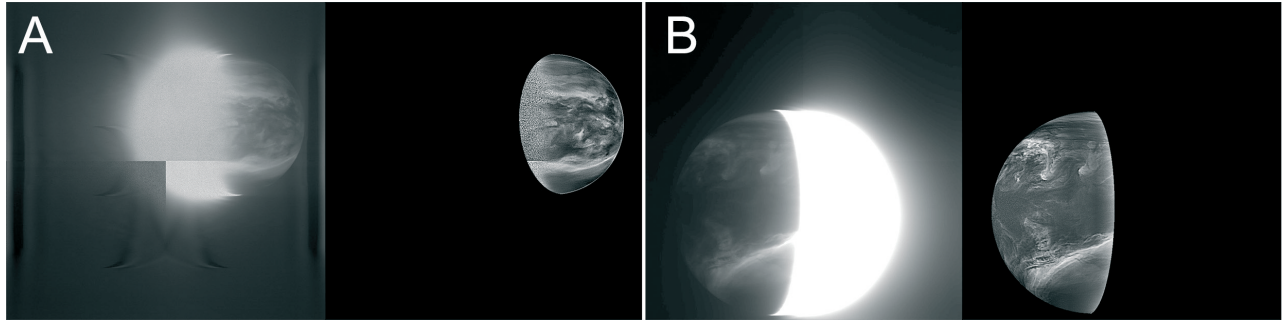


Figure 1. Examples of IR2/2.26- μm images before and after the processing procedure described in this work: **(A)** IR2 image acquired in March 25, 11:33 UT, and **(B)** IR2 image acquired in August 25, 04:03 UT. Both images have been oriented so that the north-south-west-east of Venus appears approximately oriented up-down-left-right in the image.

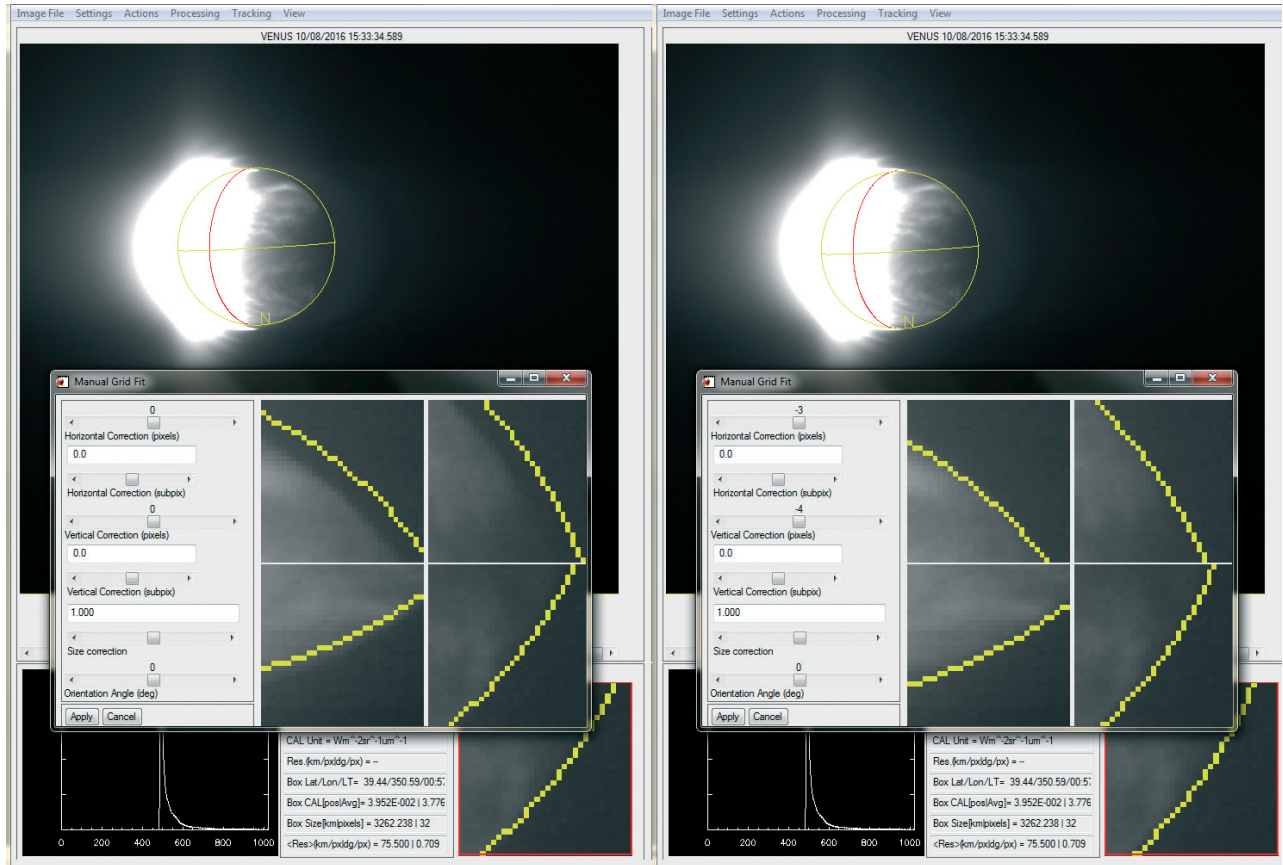


Figure 2. Example of the correction on the navigation of Akatsuki images using as reference a set of locations of the planetary limb selected by the user. The original navigation grid and the corrected one are displayed on the left and right sides, respectively.

justment using an automatic template matching which is visually accepted or rejected by the human operator (similarly as performed by Hueso et al. 2015); and (b) a *fully-automatic method* used for images taken in 2016 July and August (see Table 1) and which applies the relaxation labeling technique (Ikegawa & Horinouchi 2016; Horinouchi et al. 2017a).

Wind measurements are obtained by comparing the position on maps of cloud features that can be identified in two consecutive images with a given time difference. We obtained wind measurements with a *manual method* in which we perform an automatic template matching with a *phase-correlation* technique that has been also applied for cloud tracking on the Earth (Leese et al. 1970; Jun & Fengxian 1992; Humblot et al. 2005; Huang et al. 2012). We call this technique *manual* because a

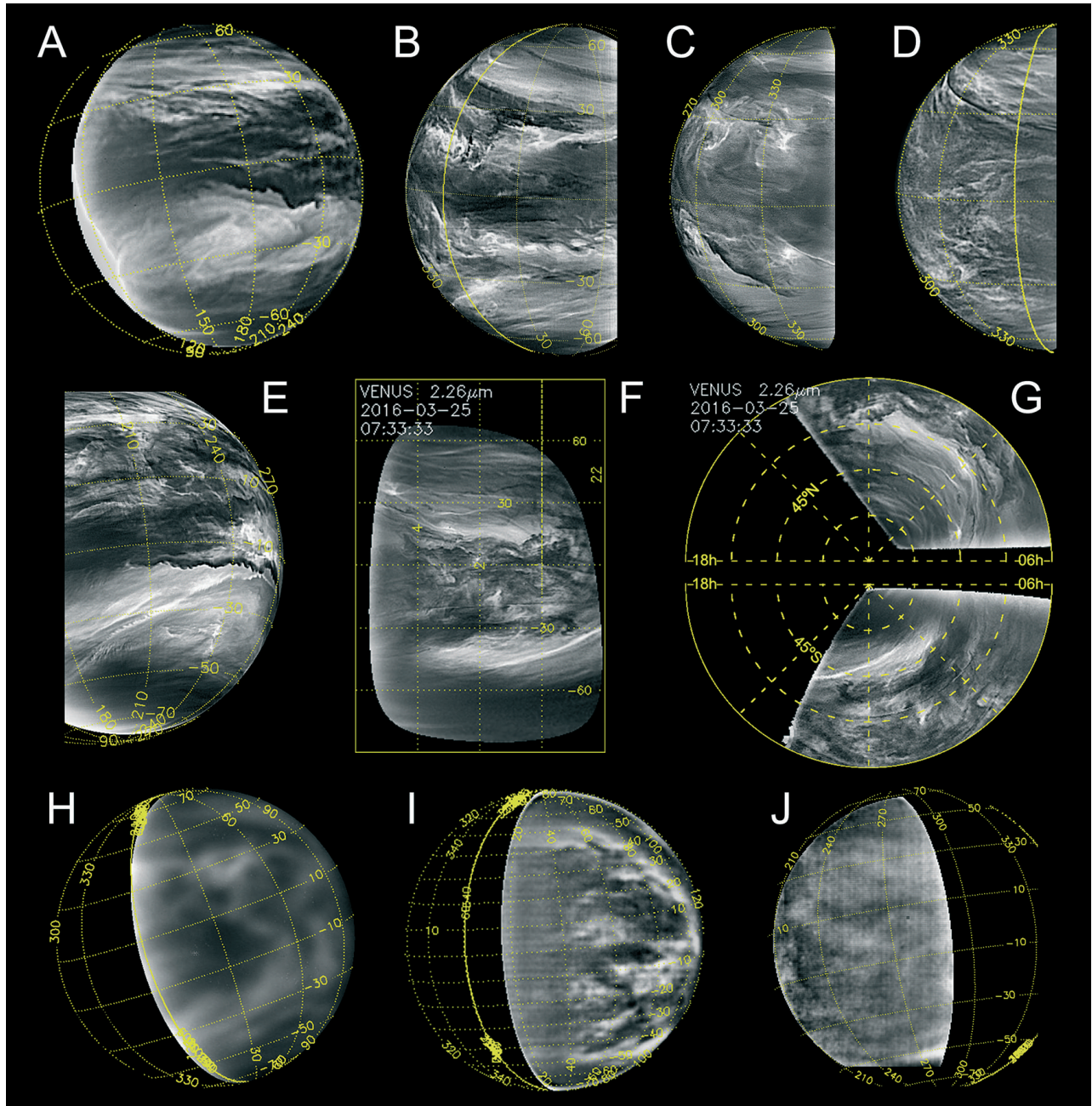


Figure 3. Examples of images acquired with the filter $2.26\text{-}\mu\text{m}$ by Akatsuki/IR2 during the year 2016 (A–G) and ground-based observations at $2.32\text{-}\mu\text{m}$ from TNG/NICS and IRTF/SpeX (H–J): (A) 2016 October 10, 09:23 UT, (B) 2016 August 13, 00:33 UT, (C) 2016 July 11, 22:03 UT, (D) 2016 July 22, 14:33 UT, (E) 2016 October 19, 14:33 UT, (F) cylindrical and (G) polar projections for 2016 March 25, 07:33 UT (original shown in Fig. 6A), (H) 2012 July 11, 05:19 UT by TNG/NICS, (I) 2015 September 28, 16:03 UT by IRTF/SpeX, and (J) 2017 February 10, 02:31 UT by IRTF/SpeX. In the case of the polar projection (G), the northern and southern hemispheres are displayed above and below, respectively, with the geographical north/south pole located in the center.

human user selects a region in the first image to obtain its best match in the second image and validates (or not) the final result. The phase-correlation permits to obtain the translation between two images shifted relative to each other (Kuglin 1975; Samritjarapon & Chitsobhuk 2008), relying on a frequency-domain representation of the images calculated with the Fast Fourier Transform that enables to infer this shift from the location of a peak in a *cross-correlogram*. Figure 4 shows an example of the use of this technique where the narrow peak in the phase cross-correlogram is shown for a well identified tracer. A more complete explanation about the phase-correlation is provided by Kuglin (1976). Compared to the standard correlation, its performance is faster, and it is less sensitive to random noise and illumination conditions (Ahmed & Jafri 2008). Even though the phase-correlation can potentially register sub-pixel displacements (Reddy & Chatterji 1996; Foroosh et al. 2002), we did not test this capability in this work and only accounted for displacements expressed as integers of pixels. Besides, since the boundaries of any image imply discontinuities in the signal that can introduce a noisier result, a zero-padding is advisable before applying the FFT (Ahmed & Jafri 2008). For this reason, the initial and final templates (ranging sizes of 32×32 to 48×48 pixels) were convolved with a Hanning window with a width of 0.7 before the FFT was applied. When no clear peak could be found with the phase correlation, or when the tracer identification was judged as not satisfactory for the human operator running the analysis, the wind measurement was rejected and the template matching was performed manually. Each of these manual measurements was verified by a human operator looking at visual reports as the one shown in Figure 4.

A fully automatic technique based on classical image correlation for identifying the cloud tracers motions was also used by Horinouchi et al. (2017a,b) and we will show here detail report of these measurements. This technique is similar to those used in many previous studies of Venus cloud dynamics (Rossow et al. 1990; Kouyama et al. 2012; Khatuntsev et al. 2017; Horinouchi et al. 2018), but in this case the cross-correlation between images is computed along a sequence of images to estimate the horizontal velocity at a specific location (Horinouchi et al. 2017b, see Methods therein). This method was applied to images of the lower clouds acquired in 2.26 and $1.74\text{-}\mu\text{m}$. All the IR2 images were projected onto equirectangular geometry with a fixed angular resolution of 0.125° per pixel regardless of the resolution of the original images (Ogohara et al. 2017).

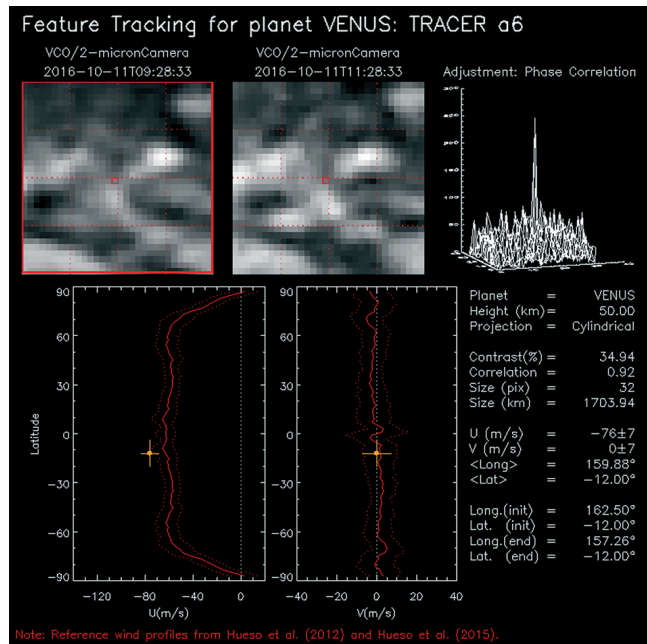


Figure 4. Example of positive identification of a cloud tracer in a pair of IR2 images using phase-correlation. Note that when a match is successful (see templates), a single and clear peak—ideally Kronecker delta—is apparent in the cross-correlogram located in the corner right-up. The inferred wind speeds are compared with a reference wind profile from VEx/VIRTIS-M (Hueso et al. 2012) in the two graphs below, while detailed information is provided on the right side below the correlogram. A complete report of clouds’ matches with phase correlation can be found in the Supplemental Material (see Appendix A).

Image processing was applied after the projection and consisted on a two-dimensional bandpass filter with Gaussian functions with the sigma values 0.25° for low pass and 3° for high pass with latitude and longitude. Finally, the template size for cloud tracking was set to a fixed value of 60×60 pixels for all the images.

3. MERIDIONAL PROFILES OF WIND SPEEDS

A total of 2,947 wind vectors were obtained with the manual method for the nightside images of the IR2 camera for the full period covering during 2016 from March 22 (when pairs of IR2 images were taken within the same day for the first time) until October 31. The spatial resolution of the images ranged 10–80 km per pixel and we selected pairs of images with time separations ranging from 1 hour up to 22 hours (in special cases of clouds displaying very small deformations over large time scales). The size of the cloud tracers comprise dimensions ranging 510–2,550 km, depending on the spatial resolution selected for the geometrical projections. Images acquired over 2016 April, July and

August were also independently measured with the fully-automatic method described above resulting in 149,033 wind measurements from the tracking of cloud features with a fixed size of 790 km. The errors for the wind speeds obtained with manual tracking were calculated from the spatial resolution and the time interval between the images as explicated by [Bevington & Robinson \(1992\)](#), while in the case of automatic cloud tracking the calculation of the errors are explained by [Ikegawa & Horinouchi \(2016\)](#).

[Satoh et al. \(2017, fig. 11b therein\)](#) and [Limaye et al. \(2018, fig. 15 therein\)](#) show Akatsuki IR2 images of strong cloud discontinuities in the lower clouds of Venus. These discontinuities propagate faster than the background zonal flow and were suspected to be the manifestation of waves rather than passive tracers. For this reason, we discarded the motions of these strong opacity discontinuities from our study of the global wind motions. In the case of the automatic cloud tracking, we ruled out all the measurements obtained from image pairs where this equatorial cloud discontinuity was apparent. As a result of this filtering, the number of wind vectors with the manual and automatic methods was reduced to 2,277 and 101,882 respectively. Since the automatic method does not provide a registry of the cloud morphologies tracked, this filtering also removed all automatic-generated wind vectors during April 2016. [Table 1](#) summarizes the results obtained with both techniques in different time periods and their coverage over the planet. The full report of wind measurements from the 2.26- μm IR2 images without filtering out specific features and obtained with the manual method can be found in the Supplemental Material (see [Appendix A](#)), including a table with the complete data set of wind measurements with manual tracking, geometrical projections, animations and detailed template matching results.

3.1. Morphologies of the nightside clouds

Panels **A–G** in [Figure 3](#) exhibits a sample of the clouds' morphologies observed in the IR2/2.26- μm images. Pioneering ground-based observations at these wavelengths ([Allen & Crawford 1984](#); [Crisp et al. 1991](#)) show similar global characteristics as Akatsuki IR2 images. The deeper clouds of Venus nightside are normally characterized by a dark band with high opacity clouds at low latitudes, while the mid-latitudes are dominated by brighter bands with lower opacity (see [Figs. 3A–B](#)). Prior to Akatsuki, the mid-latitude bands appeared as almost featureless ([Crisp et al. 1991](#); [Limaye et al. 2006](#);

[Hueso et al. 2012](#)). However, the higher spatial resolution of the Akatsuki IR2 images reveals on them subtle though distinguishable wisps and patches ([Figs. 3F–G](#)) sometimes invaded by broad bands of clouds with higher opacity ([Fig. 3B](#)), or unusual sharp dark spirals tilted relative to the latitude parallels ([Figs. 3C–D](#)) which spread thousands of kilometres from latitudes higher than 30° towards equatorial ones ([Horinouchi et al. 2017b](#); [Satoh et al. 2017](#); [Limaye et al. 2018](#)).

In the IR2 images, the clouds' opacity at lower latitudes exhibits higher variability than at mid-latitudes ([Satoh et al. 2017](#); [Limaye et al. 2018](#)), confirming previous findings with ground-based observations ([Crisp et al. 1991](#); [Limaye et al. 2006](#); [Tavenner et al. 2008](#); [Mota Machado et al. 2016](#)) and during the VEx mission ([Hueso et al. 2012](#); [McGouldrick et al. 2012](#); [McGouldrick & Tsang 2017](#)). Dark areas of high opacity normally dominate lower latitudes, while their boundary with the mid-latitude bright bands exhibits complex cloud features ([Horinouchi et al. 2017b](#); [Limaye et al. 2018](#)), like small vortices or abundant bright swirls at around 30° which sometimes adopt shapes suggestive of shear instabilities ([Fig. 3B,C,E](#)), similar to those found at the nightside upper clouds at ~ 65 km with 3.8- μm VEx images ([Peralta et al. 2017c](#)). The polar projection in [Fig. 3G](#) clearly exhibits an example of the frequent episodes of hemispherical asymmetry for the Venus clouds' morphology. A more complete survey of the clouds' morphologies apparent in the images by the Akatsuki/IR2 camera will be presented elsewhere.

3.2. Latitudinal profiles of the winds and relation with clouds

[Figure 5](#) shows zonally-averaged profiles of the manually-tracked winds at the lower clouds during the first year of Akatsuki observations. Bins of 5° of latitude were considered to calculate average wind speeds from March to October 2016. The profiles of IR2 are compared with VEx/VIRTIS-M results from 2006 April to 2008 August ([Hueso et al. 2012](#)). With regards to the zonal component of the wind ([Fig. 5A](#)), the mean profile obtained with IR2 is faster than VIRTIS-M measurements by 10 ms^{-1} . The zonal winds from IR2 observations show symmetric profiles between both hemispheres and, despite the higher dispersion at higher latitudes due to the poorer spatial resolution of the IR2 images close to the poles, they show for the first time the decay of the winds towards the poles on both hemispheres simultaneously. This decay starts at about 60° and, compared to VEx results, it seems more abrupt,

Table 1. Coverage of Akatsuki/IR2 Winds during year 2016

Month	Dates*	Latitudes	Local Times	Longitudes	Wind Vectors**
March	22,23,25–30	61°N–60°S	23h–05h	225°–308°	249
April	15	43°N–63°S	01h–06h	281°–348°	35+ 306
June	20	40°N–21°N	18h–20h	264°–289°	12
July	1, 11 ,12,22	72°N–69°S	18h–01h	250°–23°	308+ 6920
August	2,9,10,13,15–17 , 18,19, 20,21,22,25 , 26,27,28,29,30	58°N–58°S	18h–03h	322°–129°	1057+ 94656
September	4–6,15,26,27	59°N–60°S	19h–05h	28°–188°	347
October	2–7,10–17, 19–27,31	56°N–72°S	20h–05h	114°–270°	939

*Bold characters stand for dates with wind measurements from both manual and fully-automatic methods. Normal characters are used for dates with only manual measurements.

**Normal and bold characters stand for number of wind measurements obtained with the manual and fully-automatic methods, respectively.

while it keeps similarities with wind profiles obtained in 2004 with ground-ground observations (Limaye et al. 2006, fig. 5 therein), albeit, with higher errors. However, we cannot rule out that these differences at subpolar latitudes with respect to VEx/VIRTIS-M subpolar winds are not caused by the worse spatial resolution at polar latitudes and the low number of measurements in the Akatsuki IR2 images (Fig. 5C). Regarding the meridional component of the wind (Fig. 5B), the results of 2016 and 2006–2008 are in good agreement, confirming the absence of clear global motions in the meridional circulation of the nocturnal lower clouds.

Wind variability is also apparent during 2016 (see Fig. 6). The profile obtained in 2016 March 25 (Fig. 6A) corresponds to winds that are approximately constant between the equator and mid-latitudes with small meridional shear. This seems to be most frequent case found at the lower clouds during the Akatsuki observations and also during the VEx mission (Hueso et al. 2012, fig. 7 therein). Zonal wind profiles on other dates like the July 11 (Figs. 6B) and October 13 (6C) exhibit more intense equatorial zonal speeds, first-time reported during the Galileo flyby (Crisp et al. 1991, fig. 4 therein) and later identified as recurrent episodes of jets at the equator (Horinouchi et al. 2017b). There is a reasonable correspondence between this local intensification of the zonal speeds and the presence of features resembling shear instabilities (Fig. 6B) or sharp opacity discontinuities at the equator (Fig. 6C). The high dispersion in

the horizontal speeds also suggests that these jets may be apparent only in a rather longitudinally narrow area. The profile during July 11 (Fig. 6B) shows that these jets can sometimes show up at northern latitudes, as also reported in 1990 during the Galileo flyby (Carlson et al. 1991, fig. 6 therein) and in 1996 from observations at the Apache Point Observatory (Chanover et al. 1998, fig. 7 therein).

4. SOURCES OF VARIABILITY FOR THE WIND SPEEDS AT THE LOWER CLOUDS.

In this section, we explore whether the size of the features tracked, the opacity of the clouds, the uncertainties in their vertical sensing, or a dependence on the local time and surface elevations, can help to explain the variability observed in the winds of the nightside lower clouds.

4.1. Effect of opacity and size of the clouds

It is yet unclear whether the episodes of faster zonal speeds shown in Fig. 6 may be related to horizontal and/or vertical gradients of the zonal wind, or if the bright and dark clouds observed on the nightside at 1.74, 2.26 and 2.32 μm are moving at the same or at slightly different vertical levels. Early interpretations of Venus IR features considered that these clouds' contrasts might be caused either by scattered sunlight leaking in from the dayside along altitudes with low absorption in the CO₂ windows, or that dark areas

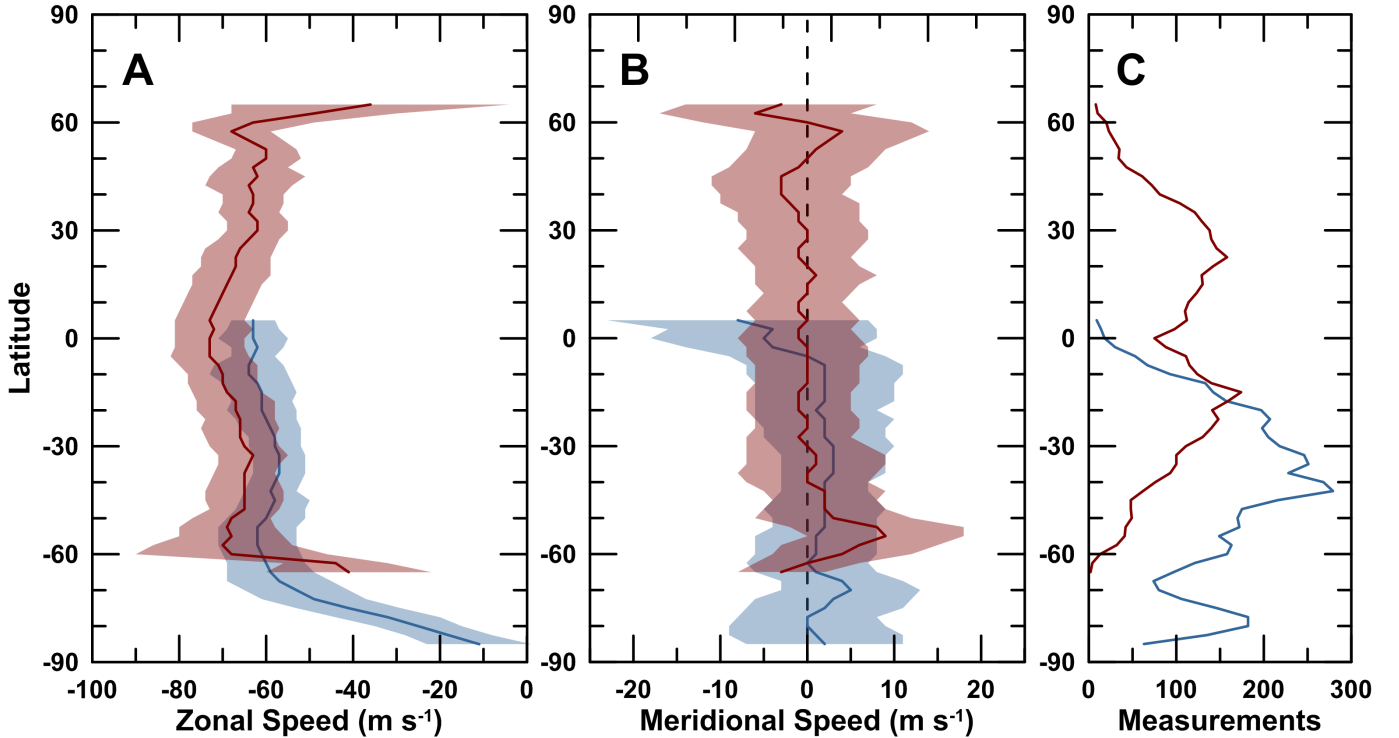


Figure 5. Mean profiles of the winds at the nocturnal middle-to-lower clouds of Venus as measured from March to October 2016 with the manual method using the Akatsuki/IR2 2.26- μm images (dark red line). These profiles are compared with the winds measured with 1.74- μm images acquired with VEx/VIRTIS-M (blue line) between 2006 April and 2008 August (Hueso et al. 2012). The profiles for the zonal and zonal and meridional components are shown in panels (A) and (B), respectively. Average values shown here were calculated for bins of latitude of 5° , and the number of measurements used in each bin are displayed in panel C. The shadowed areas stand for the standard deviation at every latitude bin when this is larger than the measurement error computed from the image resolution and time differences in the image pair.

corresponded to opaque clouds lying in a broken layer at certain altitude above the brighter regions and radiate as blackbodies at the lower temperature of their tops (Allen & Crawford 1984). Allen (1987) discarded both interpretations, confirming that the existence of important differences in the vertical elevation of bright and dark clouds was inconsistent with the small variations that dark/bright areas exhibit in CO absorptions affecting the wide 2.2-2.3 μm band. Therefore, the dark and bright regions should correspond to horizontal inhomogeneities in the clouds' opacity to the deeper background thermal emission (Allen 1987; Crisp et al. 1989), although certain discrepancies of altitude between dark and bright clouds cannot be discarded since these inhomogeneities can be caused by variations in the size and distribution of the particles within the lower and middle clouds (McGouldrick & Toon 2008).

Assuming a range of 50–60 km for the altitudes sensed at the relevant wavelengths (McGouldrick et al. 2008), a comparison with *in situ* wind profiles from descending

probes (Gierasch et al. 1997; Counselman et al. 1980; Moroz & Zasova 1997) indicates that variations of up to 30 m s^{-1} could be explained in terms of the vertical shear (Peralta et al. 2017c, fig. 3 therein), what is also consistent with the magnitude of the reported jets (Horinouchi et al. 2017b, fig. 2b therein). Crisp et al. (1991) obtained a discrepancy between velocities of large dark clouds and the smaller markings (sizes ranging 400–1000 km), and also suggested that these might be produced at different altitudes. Figure 7 displays the distribution of zonal speeds obtained with the manual method compared with the averaged radiance (Fig. 7B) and the size of the cloud tracers between 50°N – 50°S (Fig. 7A) in the IR2 2.26- μm images. No dependence is apparent between the zonal velocities and these parameters. Since the low latitudes frequently exhibit cloud patterns that resemble shear instabilities for a wide range of scales (see Figs. 3C–E; Limaye et al. 2018, fig. 10 therein), the generation of jets due to meridional gradients in the horizontal winds seems probable. McGouldrick & Toon (2007, 2008) showed that large-scale dynamics can also

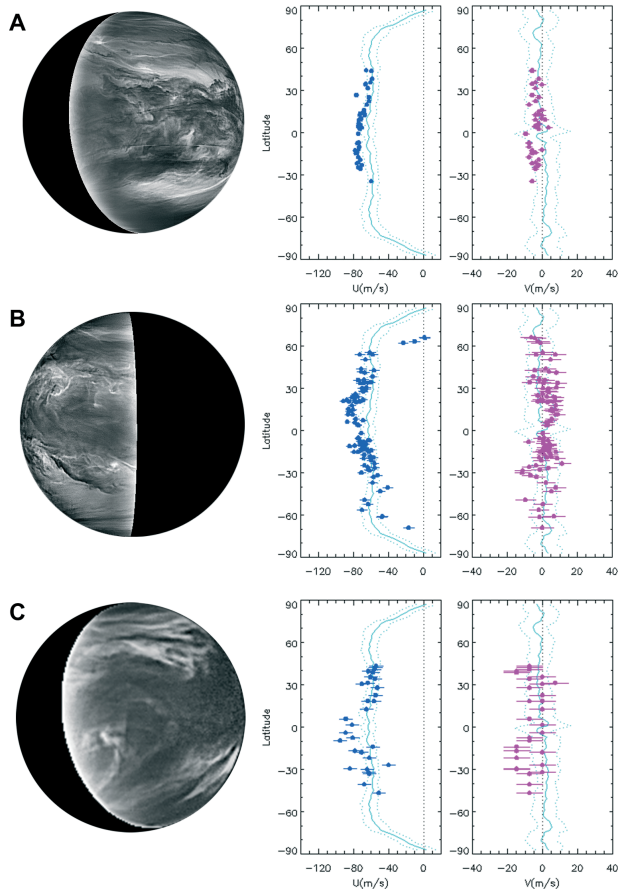


Figure 6. Variability in clouds’ morphology (left column) and profiles of zonal and meridional winds (center and right column) during the Akatsuki mission in 2016: (A) winds during March 25, exhibiting the standard profile of constant zonal speeds; (B) winds during July 11, displaying a zonal jet at $\sim 20^\circ\text{N}$; and (C) winds during October 13, exhibiting a strong jet at the equator and higher dispersion in the southern hemisphere. Reference profiles built from winds during the VEx mission (Hueso et al. 2012) and plot in a symmetric way for the two hemispheres are displayed in cyan.

explain the strong variations in the cloud opacity, and that even weak downwelling is able to produce optical-depth holes in the clouds.

4.2. Local time dependence.

Since most of the sunlight absorption occurs on Venus within the clouds’ layer, solar tides are expected to be excited and carry momentum away upwards and downwards from the region of excitation, thus accelerating the atmosphere westwards and contributing to the RZS (Gierasch et al. 1997; Sánchez-Lavega et al. 2017). The effect of the solar tides have been unambiguously detected on both zonal and meridional components of the winds at the upper clouds at 65–70 km (Rossow

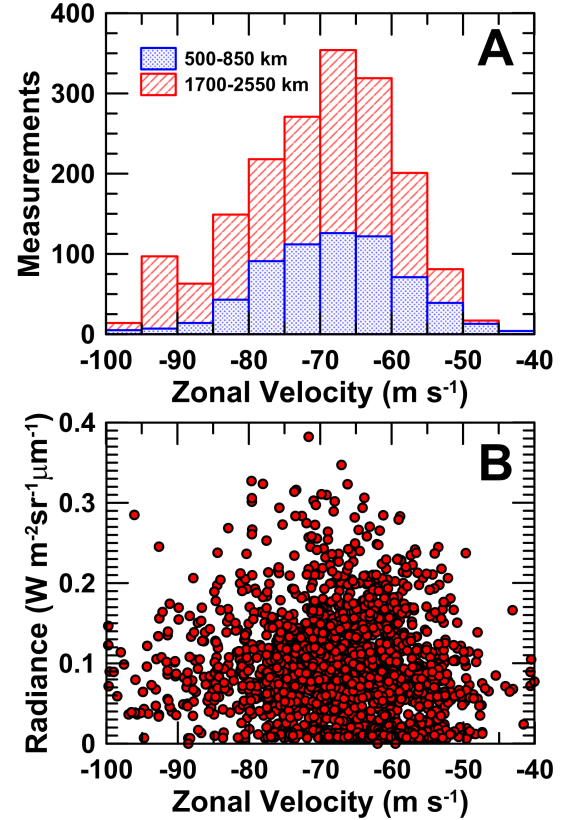


Figure 7. Histograms and scatter plot of the wind measurements acquired with the manual method and Akatsuki/IR2 images. The panel (A) shows histograms of the zonal velocities for two ranges of spatial scales of cloud tracers. The panel (B) exhibits the values of zonal wind speeds in terms of the mean radiance (red dots). The radiance is given for the calibration version “v20170601” of the IR2 2.26- μm images, and corresponds to the radiance averaged inside the template.

et al. 1990; Limaye 2007; Sánchez-Lavega et al. 2008; Kouyama et al. 2012; Peralta et al. 2012; Khatuntsev et al. 2013; Hueso et al. 2015), but no evident influence has been found for the middle-to-lower clouds (50–60 km) for either day (Hueso et al. 2015; Khatuntsev et al. 2017) or night (Hueso et al. 2012, fig. 6 therein). Khatuntsev et al. (2017) argued that this negligible effect of the solar tides could be related to the absence of the unknown absorber downward of the middle clouds (which is responsible for most of the solar heat deposition on Venus).

Figure 8 allows to study the local time dependence for the winds at the nightside lower clouds of Venus during 2016. In agreement with VEx results during 2006–2008, no local time dependence is apparent in the meridional

winds (Fig. 8B). However, the zonal component of the wind speed displays a local increase of the zonal speeds between 19–22 LT, followed by a gradual decrease towards late nightside local times (decrease of $\sim 10 \text{ m s}^{-1}$ between 19 LT and midnight). Hueso et al. (2012) also reported hints of faster retrograde winds close to dawn during 2006–2008, although this local time effect was weaker and disregarded due to the small number of measurements in this area. Recent results from Venus General Circulation Models (h.a. GCMs) predict that the diurnal tide should be also apparent on the zonal wind down to the middle clouds at $\sim 60 \text{ km}$ with the slowest speeds centered at the evening terminator (Takagi et al. 2018, fig. 3a therein). Better agreement is found for the GCM results at the lower clouds ($\sim 50 \text{ km}$), where the influence of the diurnal tide is predicted to weaken but a local maximum of about 10 m s^{-1} is also found in the early night and before the midnight (Takagi et al. 2018, fig. 4a therein).

4.3. Longitudinal dependence.

Evidences on how the surface topography may be influencing the atmospheric circulation through the excitation of atmospheric stationary waves (lee waves) have been accumulating. Vertical disturbances experienced by the VEGA-2 balloon over Aphrodite terra (Blamont et al. 1986), strong asymmetries of the water vapor over certain geographical locations (Fedorova et al. 2016), or the finding of multiple stationary waves at the upper clouds of Venus which are strongly correlated with the surface elevations (Peralta et al. 2017c; Fukuhara et al. 2017; Kouyama et al. 2017) strongly suggest surface effects on the upper atmosphere. Results of cloud tracking in VEx/VMC dayside images seem to support that the wind speeds at the cloud tops are decelerated as they pass over Aphrodite terra and Atla regio (Bertaux et al. 2016, figs. 4 and 6 therein). Other works have reported indications of an effect of surface elevations for the winds at the middle cloud (Khatuntsev et al. 2017, fig. 14 therein) and over the oxygen airglow patterns (Gorinov et al. 2018).

Peralta et al. (2017c) discovered that during 2006–2008 the RZS at the nocturnal upper clouds exhibited a higher variability compared to the dayside, but the geographical coverage of the wind measurements was insufficient to confirm a correlated effect with the surface elevations. In the case of the lower clouds on the nightside, stationary waves are paradoxically missing in the clouds’ opacity and no longitudinal dependence had been reported for the wind speeds (a reanalysis

of VIRTIS-M winds for the lower clouds resulted inconclusive due to the lack of enough data to separate local time effects from time variability and the elusive surface dependence). Figure 9 displays the dependence on the longitude and latitude for the manual wind measurements with the Akatsuki IR2 images. While no clear effect is found for the meridional component of the wind (Fig. 9B), the westward windspeeds exhibit a local maximum at low latitudes over longitudes ranging 300° – 120° (fig. 9A).

Unfortunately, separating the effects of the longitudinal and local time dependences is not feasible with our results, since the observed velocity disturbances are just marginally larger than the corresponding errors and the incomplete coverage of our wind measurements. Figure 10 shows the distribution of the mean zonal speeds (panel 10A) and the number of measurements (10B) in terms of local time and longitude. To avoid the expected decrease of the zonal winds towards the poles, only the Akatsuki/IR2 wind measurements between 50°N – 50°S were considered. Panel 10B shows that the number of wind measurements during the year 2016 is irregularly distributed for both longitude and local time parameters, preventing a confirmation of either a local time dependence and/or influence of surface elevations.

However, the influence of the surface elevations over the zonal winds at the nightside lower clouds might be yet regarded as controversial. Published results for the zonal winds on the dayside were originated from a huge set of wind measurements with noticeable dispersion (Bertaux et al. 2016, fig. 2 therein), and authors do not report filtering out other important sources of variability such as transient waves or the local time dependence. In the case of zonal wind speeds obtained with Akatsuki/UVI images, Horinouchi et al. (2018) characterized and removed the local time dependence on the zonal winds at the dayside upper clouds. As a result, no effect of surface elevations was found for the dayside winds (Horinouchi et al. 2018, fig. 14b therein). In the case of our results for the nightside lower clouds, the local maximum extends mostly over rather plain areas and do not seem well correlated with the surface elevations at lower latitudes. Moreover, our results seem inconsistent with those on the dayside reported by Bertaux et al. (2016) and Khatuntsev et al. (2017) since, conversely to the zonal wind speeds on the dayside from VEx/VMC which exhibit a local minimum with slower speeds extending along 0° – 200° (Bertaux et al. 2016, fig. 3 therein), our westward winds on the nightside dis-

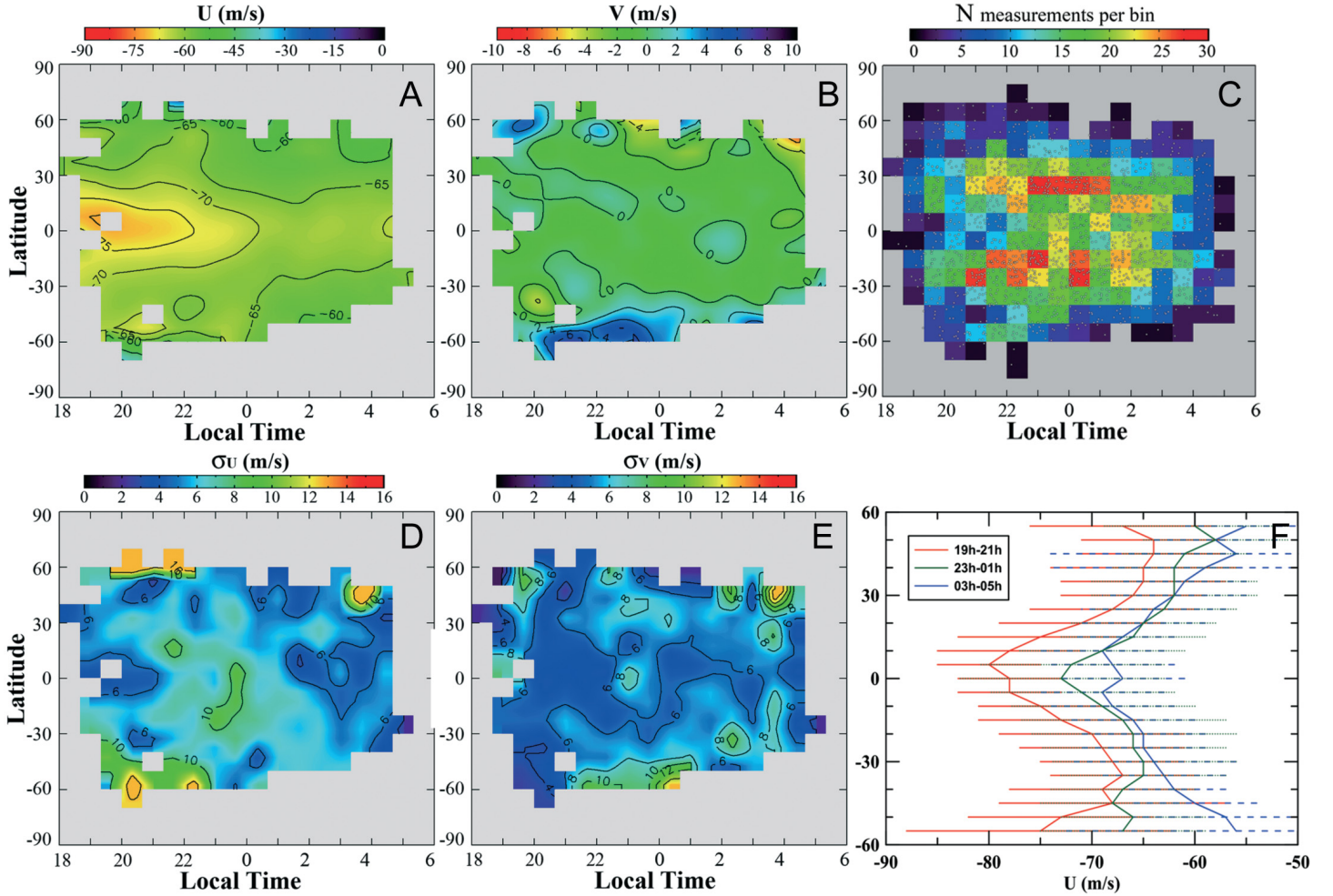


Figure 8. Local time dependence for the zonal winds obtained with the manual method on the Akatsuki/IR2-2.26- μm images. Bins of 10° in latitude and 40 minutes in local time were used. Panels (A) and (B) display the values of zonal and meridional components of the wind averaged in each bin; panel (C) shows the distribution of wind measurements with dots representing individual measurements; (D) and (E) display the standard deviation of the measurements in each bin; and (F) shows the meridional profiles of zonal winds at different intervals of local time.

play a local maximum between longitudes 300° – 120° .

4.4. Results from automatically retrieved winds during 2016 July and August

We now explore possible wind dependencies with the factors shown above for our wind results obtained in the automatic cloud correlation technique and firstly reported by Horinouchi et al. (2017b). The dependence with both local time and longitude for the winds obtained with the fully-automatic method are displayed in Figure 11. Since for these wind speeds only IR2 images obtained during 2016 July and August were used (see Table 1), the coverage is more limited than in the case of the manual method, and the dispersion is smaller than for the manual results (see figs. 8D,8E,9D and 9E).

Except for the case of the meridional winds where no clear dependence with the local time and longitude is found, the zonal winds with automatic correlation are not fully consistent with that from manual wind measurements, and no influence over the zonal speeds is observed at any range of local time or longitude. Even though some discrepancies were expected between both cloud tracking methods and the different techniques to correct the navigation of the IR2 images, the homogeneity found for the zonal winds at low latitudes might be explained due to the recurrence of the equatorial jet during August 2016 (Horinouchi et al. 2017b), which would mask a weaker dependence on local time and/or longitude.

4.5. Combined results of Akatsuki and Venus Express

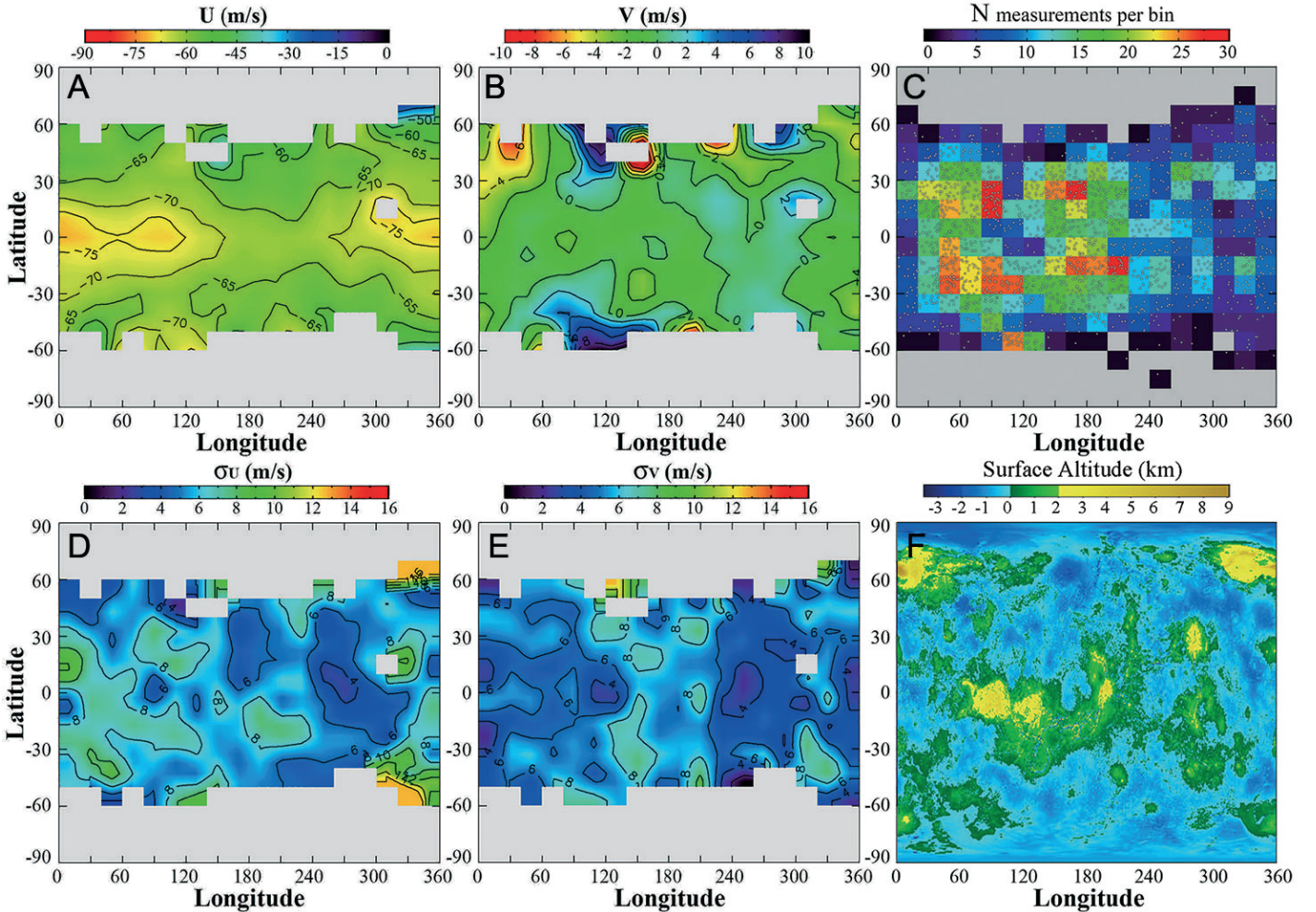


Figure 9. Local time dependence for the zonal winds obtained with the manual method on the Akatsuki/IR2-2.26- μm images. Bins of 10° and $40'$ were considered for the latitude and local time, respectively. Panels (A) and (B) display the values of zonal and meridional components of the wind averaged in each bin; panel (C) shows the distribution of wind measurements; (D) and (E) display the error (standard deviation) in each bin; and (F) exhibits the surface elevation of Venus as a comparison.

We also combined the manual wind speeds at the nocturnal lower clouds with Akatsuki/IR2 in the year 2016 with those obtained by Hueso et al. (2012) with VEx/VIRTIS-M from 2006 to 2008. Since the mean zonal winds during 2016 were faster than during the VEx mission (see Fig. 5A), the difference between the zonal averages of both datasets equatorward of midlatitudes was suppressed by multiplying by a correcting factor of 1.06 the zonal speeds obtained with the VEx/VIRTIS-M images, while those from Akatsuki/IR2 images were divided by 1.06. As a result, a correction of $\sim 4 \text{ m s}^{-1}$ was introduced in both sets of winds. Also, these two datasets have a comparable number of points and both are based on cloud tracking inspected/validated by human operators. The result of their combination is presented in the figure 12. The dependence with the local time (panels 12A–B, E–F) confirms the equatorial maximum of the zonal speeds

between local hours 18h–22h, while this dependence clearly decays towards higher latitudes. On the other hand, the meridional component of the wind displays no apparent dependence at low latitudes, while at higher latitudes of the southern hemisphere (50°S – 90°S) and between 21h–22h it exhibits an equatorward acceleration (panel 12B). These results, again, suggest that the solar tide detected on the winds of the upper clouds (Limaye 2007; Peralta et al. 2012) might be able to propagate downwards to the middle clouds as predicted by some Venus GCMs (Takagi et al. 2018). Regarding the dependence with longitude and surface elevations, the local maximum between longitudes 300° – 120° reported in subsection 4.3 for the westward windspeeds is observed (panel 12C), while the meridional component exhibits no clear influence from the surface (panel 12D).

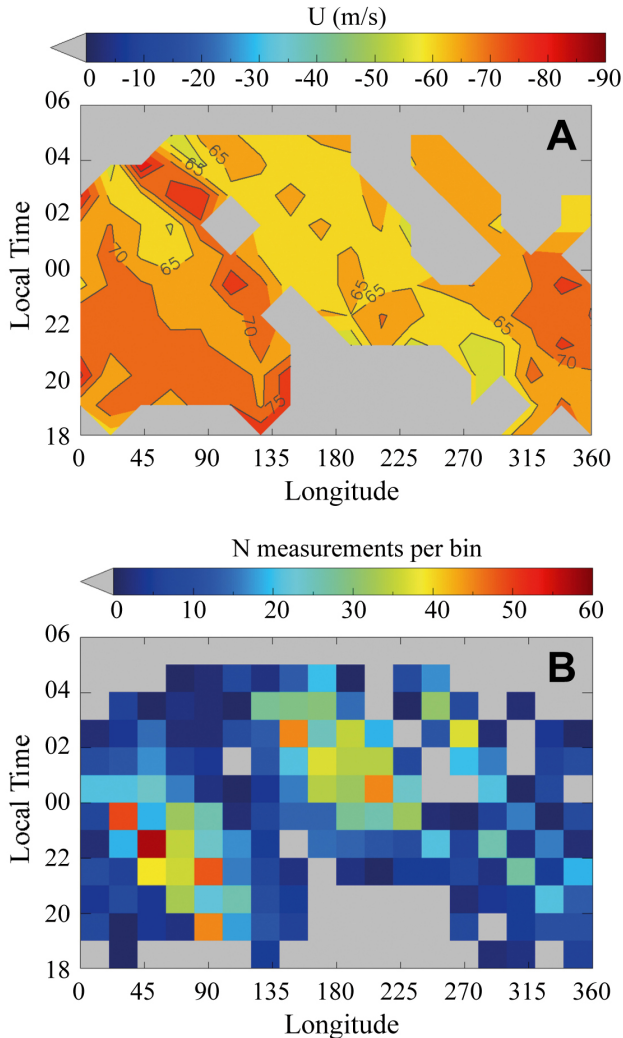


Figure 10. Distribution as a function of Longitude and Local Time of the wind measurements acquired with the manual method and Akatsuki/IR2 images between 50°N – 50°S . The panel (A) displays the distribution of the zonal wind speeds. Panel (B) shows the distribution of the number of measurements.

5. TIME EVOLUTION OF THE WINDS

Results from past space missions to Venus and comparison between them have provided evidence of long-term variability affecting the atmospheric dynamics at the upper clouds of Venus (Sánchez-Lavega et al. 2017, fig. 2 therein). Rossow et al. (1990) reported that during the Pioneer Venus zonal winds at equator and mid-latitudes exhibited variations ranging 5 – 8 m s^{-1} over time spanning 1–6 years, while the intensity of the poleward circulation seemed also subject to variability. From the analysis of the ultraviolet albedo of the cloud tops in different missions, del Genio & Rossow (1990) suggested that between 1979 and 1986

the clouds’ dynamics might experience cyclic changes with a time scale of 5–10 years. This conclusion was based on the periods of presence/absence of the 4 and 5-day wave modes, while during the VEx mission Lee et al. (2015a, fig. 18 therein) reported unexplained periods of 154, 275, 357 and 560 days on the 365-nm albedo.

Long-term trends were also observed for the dayside winds of the upper clouds during the VEx mission. Between 2006–2013 the mean zonal velocity measured with ultraviolet images from the VMC camera displayed an increase from 80 to 100 m s^{-1} at about 20°S (Khatuntsev et al. 2013, fig. 14 therein), while a similar increase trend was independently confirmed in this period with cloud tracking in VIRTIS-M images (Hueso et al. 2015). Kouyama et al. (2013) analyzed VEx/VMC images finding that the zonal winds equatorward of 30°S exhibited a periodical perturbation of ~ 10 m s^{-1} every 257 ± 2 terrestrial days which was ultimately interpreted as centrifugal waves (Peralta et al. 2014, fig. 4 therein). Measurements with Akatsuki/UVI images have also confirmed zonal windspeeds variations with time scales of ~ 100 days between December 2015 and March 2017 (Horinouchi et al. 2018, figs. 8–10 therein). Numerical simulations with GCMs have also been used to predict decadal variation in the zonal winds in Venus (Parish et al. 2011).

The long-term variability of the winds at the level of the lower clouds was studied during the VEx mission on the nightside with VIRTIS-M by Hueso et al. (2012) and on the dayside with VMC by Khatuntsev et al. (2017). During the years 2006–2008, the nightside winds at the deeper clouds showed at subpolar latitudes stronger variability than at lower ones (Hueso et al. 2012, figs. 7–8 therein), while a comparison between the zonal winds during the Galileo flyby in 1990 and the 2-year average from VEx do not indicate noticeable variations except for the northern jet reported from the Galileo/NIMS images (Sánchez-Lavega et al. 2017, fig. 3 therein). McGouldrick & Tsang (2017) reported an oscillation of approximately 150 days apparent between 30°S – 60°S on the nightside clouds’ radiance of the $1.74\text{-}\mu\text{m}$ VIRTIS-M images, with this time scale being consistent with the cycle of cloud formation and evolution driven by the radiative dynamical feedback and gravitational settling of clouds’ particles. The analysis of the dayside winds with VMC from 2006 December to 2013 August ($\sim 1,200$ days) revealed long-term variations on both components of the wind at $\sim 20^{\circ}\text{S}$, with the meridional winds exhibiting a gradual increase until doubling its magnitude, while the zonal winds seemed subject to

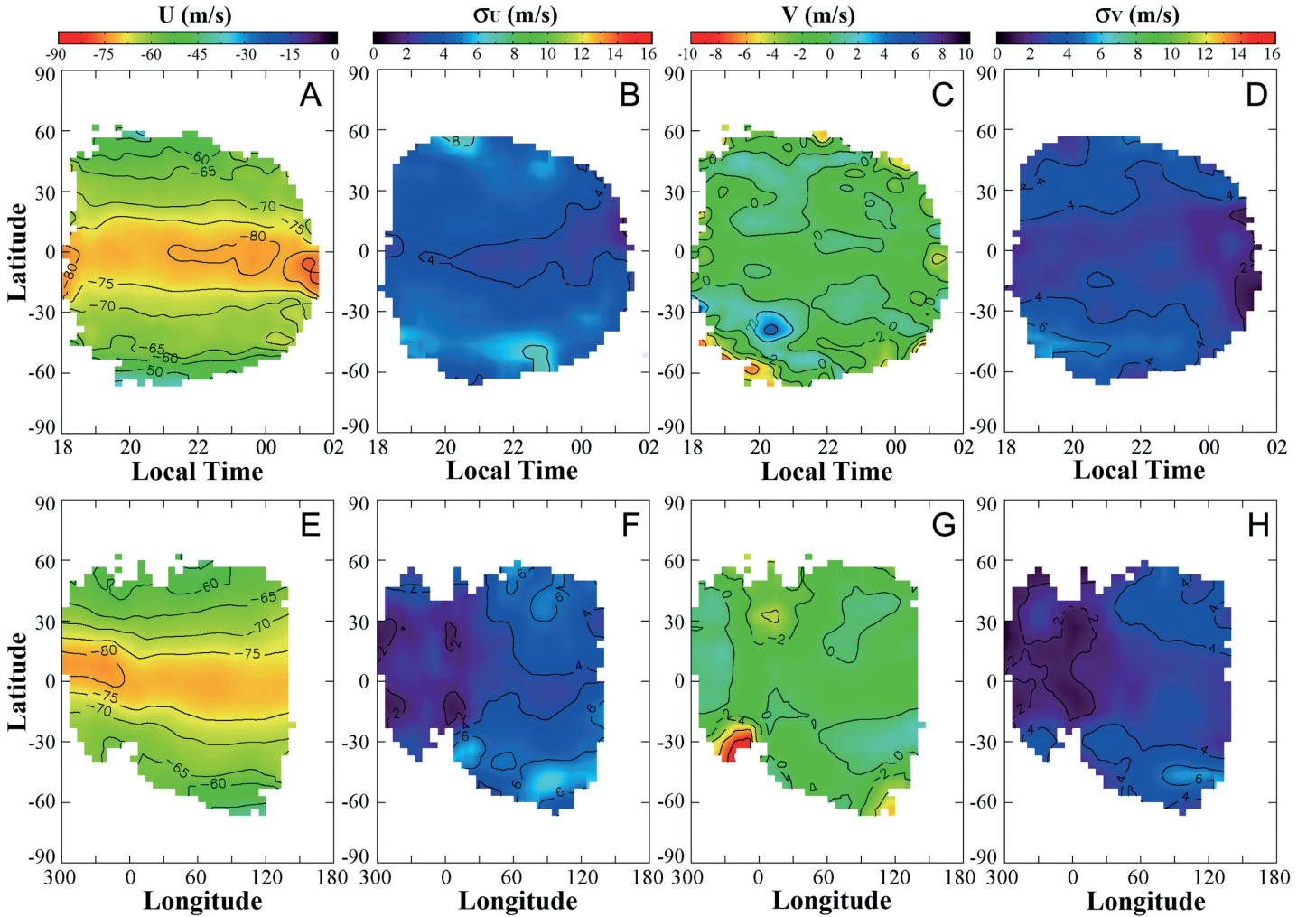


Figure 11. Contour maps for the dependence of zonal and meridional winds obtained with the full-automatic method in the Akatsuki/IR2 images. Averages (panels A,C,E,G) and standard deviation (B,D,F,H). The larger number of wind measurements allows to calculate these maps with bins of latitude, longitude and local time of 3.3° , 3.3° and 13 minutes respectively, or three times smaller than in the manual tracking results. However, the spatial coverage over local times and longitudes is more limited in this case due to the data coming from a smaller number of dates.

an apparent oscillation of ~ 3 years (Khatuntsev et al. 2017, fig. 11 therein).

In order to perform an analysis of the variability of the zonal winds at the nightside lower clouds using an even longer time scale, we decided to combine data not only from Akatsuki/IR2 and VEx/VIRTIS, but also from ground-based observations and *in situ* measurements. Figure 13 shows the variability of zonal winds at low latitudes (30°S – 30°N) of the nightside lower clouds from 1978 December to 2017 February (spanning 38 years). The zonal winds during 1978 December (Fig. 13A) and 1985 June (Fig. 13D) correspond to the averages of instantaneous *in situ* wind measurements between 50 and 60 km of altitude as provided by the Pioneer Venus Night probe (Counselman et al. 1980)

and VEGA landers (Moroz & Zasova 1997). To reduce the impact of transient phenomena like the equatorial jets, the zonal winds obtained with cloud tracking are presented as time averages of about 10–20 days in most of the cases, though this value strongly depends on the data availability and how this is distributed along time. Thus, zonal speeds from IRTF/SpEx images correspond to nearly instantaneous winds (several hours) while the average for 2004 May is provided by Limaye et al. (2006) for observations performed along 70 days. The mean zonal winds displayed in Fig. 13A–I were obtained from published results (Counselman et al. 1980; Allen & Crawford 1984; Allen 1987; Moroz & Zasova 1997; Crisp et al. 1989, 1991; Carlson et al. 1991; Chanover et al. 1998; Limaye et al. 2006). The wind speeds from 2006 to 2017 correspond to a revisit of the VEx measure-

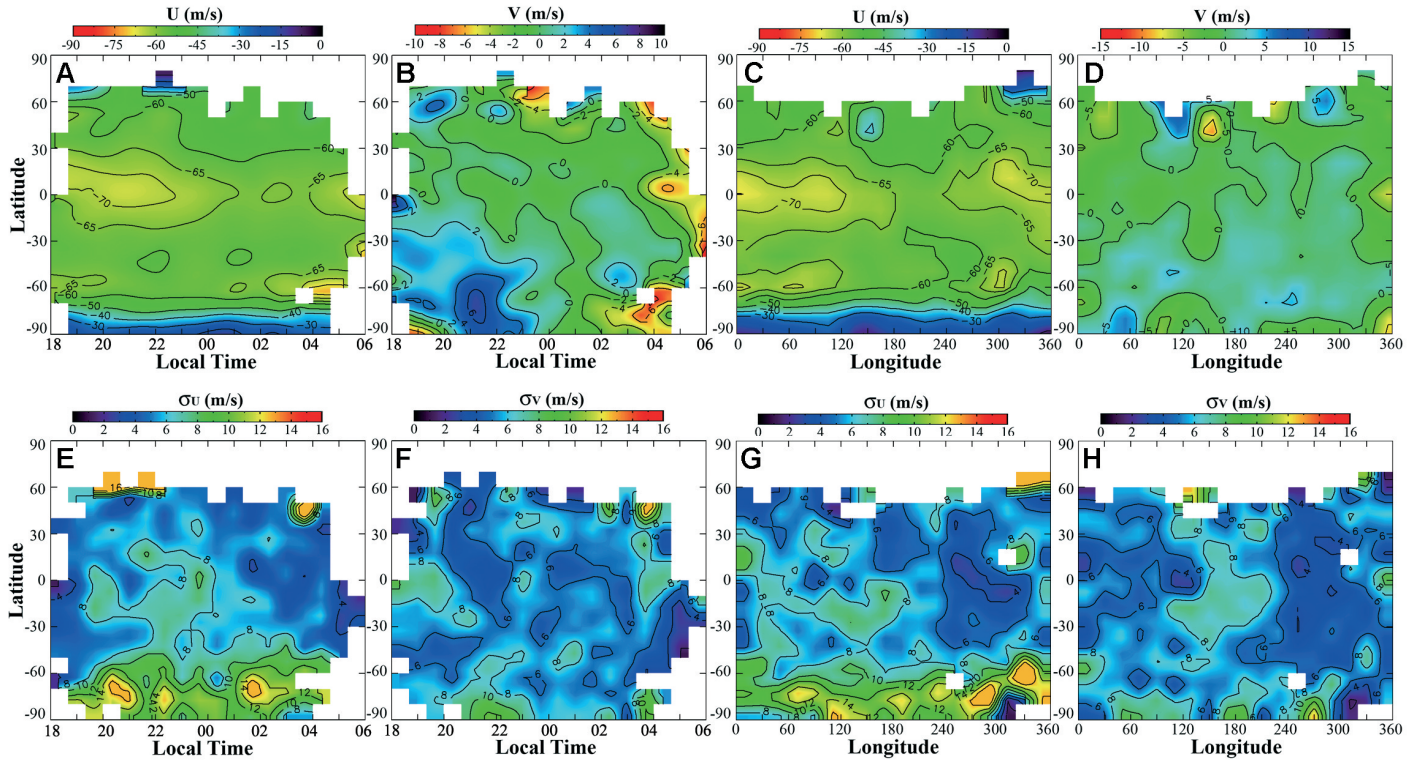


Figure 12. Winds' dependence with local time and longitude when the measurements from VEx/VIRTIS-M (2006–2008) and Akatsuki/IR2 (2016) are combined. Averages and standard deviation are calculated for bins of latitude, longitude and local time of 10° , 10° and 40° respectively. Panels (A–D) display the zonal and meridional winds' dependence with the local time and the longitude, while panels (E–H) display the corresponding errors. Since the mean zonal winds during 2016 were faster than during the VEx mission (see Fig. 5A), the zonal speeds used in panel (A) and (C) were multiplied by a correction factor to have comparable zonally averaged profiles.

ments (Fig. 13J) performed by Sánchez-Lavega et al. (2008); Hueso et al. (2012), and our measurements with Akatsuki/IR2 (Fig. 13M), IRTF/SpEX (Fig. 13L,N) and TNG/NICS (Fig. 13K).

Although caution must be taken when comparing values from different time-averages and images acquired with different filters may provide some discrepancies in the vertical level sensed, Fig. 13 suggests that the zonal wind speeds at the nightside lower clouds seem to experience long-term variation in the intensity of the winds of up to 30 m s^{-1} (this total variation is larger than variabilities linked by the local time or longitudinal dependence described in subsections 4.2 and 4.3). The zonal winds display a strong increase from the entry of the Pioneer Venus probes in 1978 (Fig. 13A) and the first cloud-tracked winds with ground-based observations (Fig. 13B) in the early 1980s. From 1983 to 1990 (Fig. 13B–G) the zonal winds exhibit a gradual decrease in magnitude, while from 2004 to 2008 the zonal winds experience an increase above the error bars (Fig. 13J from VEx data). This long-term behaviour of the night-

side zonal winds from VIRTIS-M images diverges from the oscillation between 2007 and 2009 reported on the zonal winds between 15°S – 25°S of the dayside middle-to-lower clouds found (Khatuntsev et al. 2017, fig. 11a therein). The differences between the altitude range sensed in day and night side images (Sánchez-Lavega et al. 2008; Takagi & Iwagami 2011; Khatuntsev et al. 2017) or the distinct image sampling and time coverage for the winds obtained from VMC and VIRTIS-M may account for this discrepancy between VEx results.

The decadal variability for the zonal winds at the lower clouds also keep similarities with the long-term trend for the SO_2 abundance at the cloud tops reported by (Marcq et al. 2013) during 30 years of observations combining Pioneer Venus and VEx observations. The gradual decrease of the zonal winds along 1983–1990 matches the decrease of the SO_2 at the upper clouds (Marcq et al. 2013, fig. 3 therein), what would support the idea that the vertical level sensed by the nightside images at 1.74 , 2.26 and $2.32 \mu\text{m}$ might be variable. This would make sense if the photochemical activity at

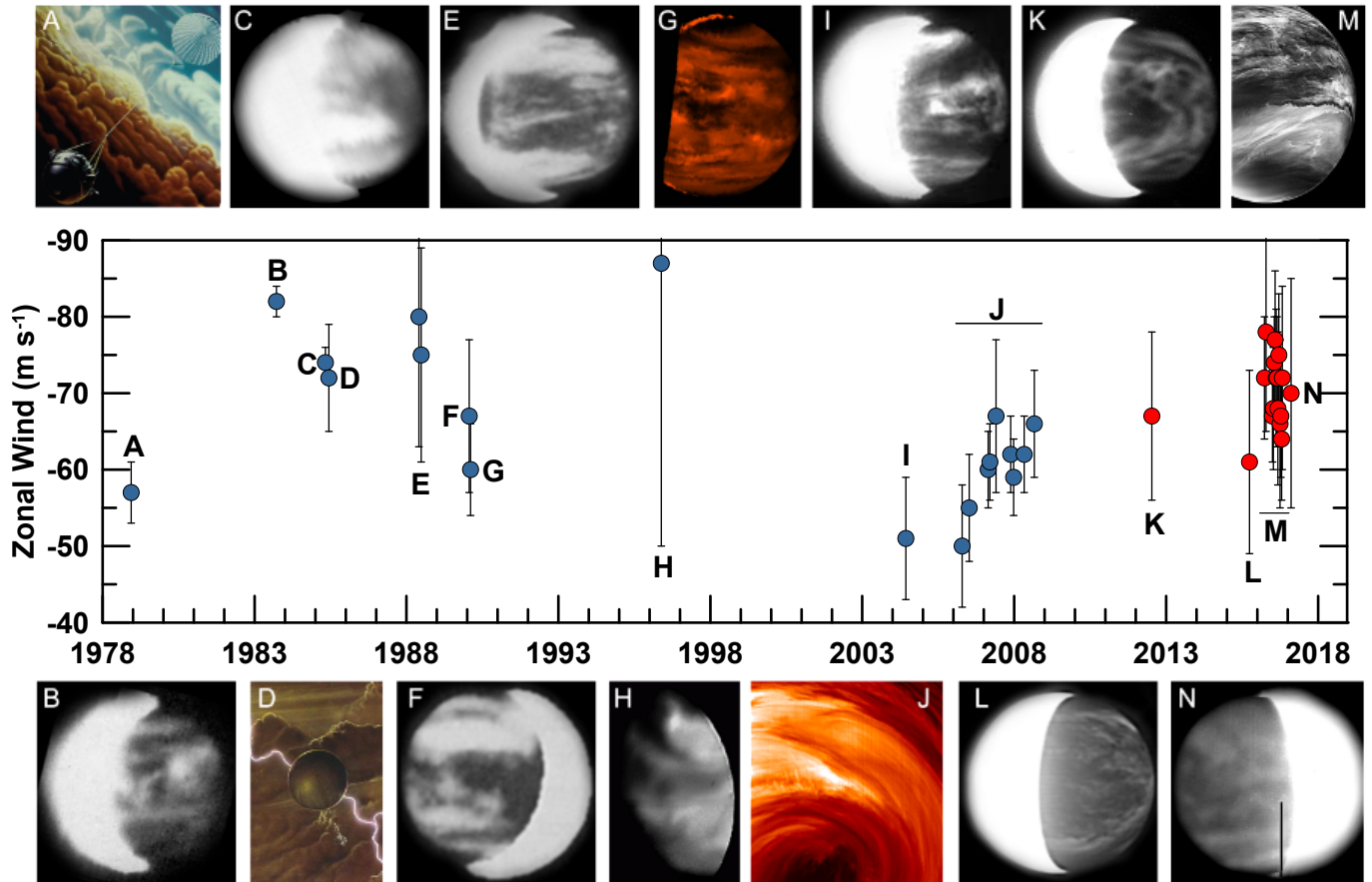


Figure 13. Decadal variation of the zonal winds at the nightside lower clouds of Venus. Data correspond to time-averages of the zonal winds obtained between 30°S – 30°N with cloud tracking, except for (A) and (D) that represent instantaneous *in situ* wind measurements from the Pioneer Venus Night probe (Counselman et al. 1980) and VEGA landers (Moroz & Zasova 1997) averaged within 50–60 km of altitude. Blue dots represent time-averages using wind speeds provided in past publications: (A) Counselman et al. (1980), (B) Allen & Crawford (1984), (C) Allen (1987), (D) Moroz & Zasova (1997), (E) Crisp et al. (1989), (F) Crisp et al. (1991), (G) Carlson et al. (1991), (H) Chanover et al. (1998), (I) Limaye et al. (2006), and (J) Hueso et al. (2012). New data presented in this work and based in cloud tracking measurements are displayed with red dots and were obtained from TNG/NICS (K), IRTF/SpEx (L and N), and Akatsuki/IR2 images (M). The error bars stand for the standard deviation of the time averages.

the upper clouds might could affect the total opacity of the cloud layer (Knollenberg & Hunten 1980; Grinspoon et al. 1993). In such a case, faster zonal speeds may be coincident with periods when higher altitudes can be sensed in the nightside images.

6. CONCLUSIONS

We have presented global results of the wind speeds at the nightside lower clouds of Venus during the first year of JAXA’s Akatsuki mission. Both zonal and meridional winds were obtained applying cloud tracking techniques over $2.26\text{-}\mu\text{m}$ images acquired by the IR2 camera from a selection of 466 images spanning the time interval

from 2016 March 22 to October 31. Automatic and manual measurements were applied independently to obtain 149,033 and 2,947 wind vectors, respectively. In the specific case of the manual measurements, the phase correlation technique was tested in the template matching for the first time on Venus with comparable results to those obtained using cross-correlation techniques in the space domain. No dependence is found between the wind speeds and the radiance or the size of the cloud tracers. This supports recent reports of wind variability due to strong horizontal shear and episodes of jets at the equator, and the identification of clouds’ morphology consistent with shear instabilities. The

meridional profiles of zonally-averaged wind speeds are in overall agreement with results during 2006–2008 from Venus Express but are systematically 10 m s^{-1} faster. Our results confirm in the northern hemisphere the expected poleward decay of the zonal winds with symmetric winds between both hemispheres. Conversely to past observations with Venus Express, zonal speeds during the Akatsuki mission exhibits a local maximum in the westward windspeeds caused by either a local time dependence and/or influence of surface elevations, although the irregular coverage of the dataset prevents a definitive confirmation of its source. Also, a first analysis of the decadal wind variability is performed for zonal winds between 30°S and 30°N using a combination of *in situ* and cloud tracking measurements performed between 1978 and 2017. Our results demonstrate yearly and decade wind variability, suggesting that the zonal winds at low latitudes might be affected by an oscillating disturbance with an amplitude of about $\sim 15 \text{ m s}^{-1}$ and a period of about 30 years.

Finally, in order to facilitate future studies of wind variability and data comparison, we provide the full data set of wind measurements performed with the manual technique, accompanied by the template match for individual measurements and animations of the projected image sequences used towards this purpose (see accompanying Supplemental Material and Appendix A).

ACKNOWLEDGEMENTS

J.P. acknowledges JAXA’s International Top Young Fellowship. R.H. and A.S.-L. were supported by the Spanish MINECO project AYA2015-65041-P with FEDER, UE support and Grupos Gobierno Vasco IT-765-13. All authors acknowledge the work of the entire Akatsuki team. We are also grateful to the anonymous reviewer for his/her useful comments to improve the manuscript.

APPENDIX

A. DESCRIPTION OF THE SUPPLEMENTAL MATERIAL

The supplemental material that accompanies this work consists on a compressed file that contains not only the numerical values for our manual wind measurements obtained with the images of Akatsuki/IR2 camera, but also a large set of images exhibiting the morphology of cloud tracers and the quality of the template matching, geometrical projections of the IR2 images and animations of the cloud motions. The contents of the supplemental material are described as it follows:

- a Readme file with a more detailed description of the contents of compressed file, as well as explanations about the naming of files and folders.
- a Microsoft Excel file with the numerical values of the 2,277 manual wind measurements and where the motions of the equatorial cloud discontinuity have been filtered out.
- a total of 103 folders for each pair of IR2 images, with wind measurements, animations and cloud tracers’ morphology and position.

REFERENCES

- Acton, C. H. 1996, *Planetary and Space Science*, 44, 65
- Ahmed, J., & Jafri, M. N. 2008, in *Image and Signal Processing*, ed. A. Elmoataz, O. Lezoray, F. Nouboud, & D. Mammass (Berlin, Heidelberg: Springer Berlin Heidelberg), 128–135
- Allen, D. A. 1987, *Icarus*, 69, 221
- Allen, D. A., & Crawford, J. W. 1984, *Nature*, 307, 222
- Baffa, C., Comoretto, G., Gennari, S., et al. 2001, *Astronomy and Astrophysics*, 378, 722
- Belton, M. J. S., Gierasch, P. J., Smith, M. D., et al. 1991, *Science*, 253, 1531
- Bertaux, J.-L., Khatuntsev, I. V., Hauchecorne, A., et al. 2016, *Journal of Geophysical Research (Planets)*, 121, 1087
- Bevington, P. R., & Robinson, D. K. 1992, *Data reduction and error analysis for the physical sciences* (New York: McGraw-Hill, —c1992, 2nd ed.)
- Blamont, J. E., Young, R. E., Seiff, A., et al. 1986, *Science*, 231, 1422
- Carlson, R. W., Baines, K. H., Kamp, L. W., et al. 1991, *Science*, 253, 1541

- Chanover, N. J., Glenar, D. A., & Hillman, J. J. 1998, *Journal of Geophysical Research*, 103, 31335
- Counselman, C. C., Gourevitch, S. A., King, R. W., Lorient, G. B., & Ginsberg, E. S. 1980, *Journal of Geophysical Research*, 85, 8026
- Crisp, D., Sinton, W. M., Hodapp, K.-W., et al. 1989, *Science*, 246, 506
- Crisp, D., McMuldrough, S., Stephens, S. K., et al. 1991, *Science*, 253, 1538
- del Genio, A. D., & Rossow, W. B. 1990, *Journal of Atmospheric Sciences*, 47, 293
- Fedorova, A., Marcq, E., Luginin, M., et al. 2016, *Icarus*, 275, 143
- Folkner, W. M., Williams, J. G., & Boggs, D. H. 2009, *Interplanetary Network Progress Report*, 178, 1
- Foroosh, H., Zerubia, J. B., & Berthod, M. 2002, *IEEE Transactions on Image Processing*, 11, 188
- Fukuhara, T., Futaguchi, M., Hashimoto, G. L., et al. 2017, *Nature Geoscience*, 10, 85
- Gierasch, P. J., Goody, R. M., Young, R. E., et al. 1997, *The General Circulation of the Venus Atmosphere: an Assessment*, ed. S. W. Bougher, D. M. Hunten, & R. J. Phillips (University of Arizona Press), 459
- Gorinov, D. A., Khatuntsev, I. V., Zasova, L. V., Turin, A. V., & Piccioni, G. 2018, *Geophysical Research Letters*, 45, 2554
- Grinspoon, D. H., Pollack, J. B., Sitton, B. R., et al. 1993, *Planetary and Space Science*, 41, 515
- Hahn, G., & Jacquesson, M. 2012, *WinJUPOS-Database for object positions on planets and the Sun*, <http://jupos.privat.t-online.de>, ,
- Horinouchi, T., Murakami, S.-y., Kouyama, T., et al. 2017a, *Measurement Science and Technology*, 28, 085301
- Horinouchi, T., Murakami, S., Satoh, T., et al. 2017b, *Nature Geoscience*, 10, 646
- Horinouchi, T., Kouyama, T., Lee, Y. J., et al. 2018, *Earth, Planets, and Space*, 70, 10
- Huang, H., Yoo, S., Yu, D., Huang, D., & Qin, H. 2012, in *Proceedings of the Twelfth International Workshop on Multimedia Data Mining, MDMKDD '12* (New York, NY, USA: ACM), 1–9. <http://doi.acm.org/10.1145/2343862.2343863>
- Hueso, R., Peralta, J., Garate-Lopez, I., Bandos, T. V., & Sánchez-Lavega, A. 2015, *Planetary and Space Science*, 113, 78
- Hueso, R., Peralta, J., & Sánchez-Lavega, A. 2012, *Icarus*, 217, 585
- Humboldt, F., Collin, B., & Mohammad-Djafari, A. 2005, in *Physics in Signal and Image Processing (PSIP) conference, PSIP '05*, Toulouse, France, 115–120
- Ikegawa, S., & Horinouchi, T. 2016, *Icarus*, 271, 98
- Iwagami, N., Sakanoi, T., Hashimoto, G. L., et al. 2018, *Earth, Planets, and Space*, 70, 6
- Jun, L., & Fengxian, Z. 1992, *Advances in Space Research*, 12, 123
- Khatuntsev, I. V., Patsaeva, M. V., Titov, D. V., et al. 2017, *Journal of Geophysical Research (Planets)*, 122, 2312
- . 2013, *Icarus*, 226, 140
- Knollenberg, R. G., & Hunten, D. M. 1980, *Journal of Geophysical Research*, 85, 8039
- Kouyama, T., Imamura, T., Nakamura, M., Satoh, T., & Futaana, Y. 2012, *Planetary and Space Science*, 60, 207
- . 2013, *Journal of Geophysical Research (Planets)*, 118, 37
- Kouyama, T., Imamura, T., Taguchi, M., et al. 2017, *Geophysical Research Letters*, 44, 12,098, 2017GL075792. <http://dx.doi.org/10.1002/2017GL075792>
- Kuglin, C. D. 1975, in *Proc. International Conference on Cybernetics Society*, 163–165. <https://ci.nii.ac.jp/naid/20001697044/en/>
- Kuglin, C. D. 1976, *Performance of the Phase Correlator in Image Guidance Applications*, Tech. rep., CONTROL DATA CORP MINNEAPOLIS MN IMAGE SYSTEMS DIV, Palo Alto Research Lab., Lockheed Missiles and Space Company, Inc., Palo Alto, California
- Lee, Y. J., Imamura, T., Schröder, S. E., & Marcq, E. 2015a, *Icarus*, 253, 1
- Lee, Y. J., Titov, D. V., Ignatiev, N. I., et al. 2015b, *Planetary and Space Science*, 113, 298
- Lee, Y. J., Sawaga, H., Sato, T. M., et al. 2017a, in *Abstracts of JpGU-AGU Joint Meeting 2017*, PPS06–P18
- Lee, Y. J., Yamazaki, A., Imamura, T., et al. 2017b, *The Astronomical Journal*, 154, 44
- Leese, J. A., Novak, C. S., & Taylor, V. R. 1970, *Pattern Recognition*, 2, 279
- Limaye, S., Warell, J., Bhatt, B. C., Fry, P. M., & Young, E. F. 2006, *Bulletin of the Astronomical Society of India*, 34, 189
- Limaye, S. S. 2007, *Journal of Geophysical Research (Planets)*, 112, E04S09
- Limaye, S. S., Watanabe, S., Yamazaki, A., et al. 2018, *Earth, Planets, and Space*, 70, 38. <https://link.springer.com/article/10.1186/s40623-018-0789-5>
- Marcq, E., Bertaux, J.-L., Montmessin, F., & Belyaev, D. 2013, *Nature Geoscience*, 6, 25
- McGouldrick, K., Baines, K. H., Momary, T. W., & Grinspoon, D. H. 2008, *Journal of Geophysical Research (Planets)*, 113, E00B14

- McGouldrick, K., Momary, T. W., Baines, K. H., & Grinspoon, D. H. 2012, *Icarus*, 217, 615
- McGouldrick, K., & Toon, O. B. 2007, *Icarus*, 191, 1
- . 2008, *Icarus*, 196, 35
- McGouldrick, K., & Tsang, C. C. C. 2017, *Icarus*, 286, 118
- Moroz, V. I., & Zasova, L. V. 1997, *Advances in Space Research*, 19, 1191
- Mota Machado, P., Peralta, J., Luz, D., et al. 2016, in *AAS/Division for Planetary Sciences Meeting Abstracts*, Vol. 48, AAS/Division for Planetary Sciences Meeting Abstracts, 115.06
- Nakamura, M., Imamura, T., Ishii, N., et al. 2016, *Earth, Planets and Space*, 68, 1.
<http://dx.doi.org/10.1186/s40623-016-0457-6>
- Ogohara, K., Kouyama, T., Yamamoto, H., et al. 2012, *Icarus*, 217, 661
- Ogohara, K., Takagi, M., Murakami, S.-y., et al. 2017, *Earth, Planets, and Space*, 69, 167
- Parish, H. F., Schubert, G., Covey, C., et al. 2011, *Icarus*, 212, 42
- Peralta, J., Hueso, R., & Sánchez-Lavega, A. 2007, *Icarus*, 190, 469
- Peralta, J., Imamura, T., Read, P. L., et al. 2014, *The Astrophysical Journal Supplement Series*, 213, 18.
<http://stacks.iop.org/0067-0049/213/i=1/a=18>
- Peralta, J., Lee, Y. J., McGouldrick, K., et al. 2017a, *Icarus*, 288, 235
- Peralta, J., Luz, D., Berry, D. L., et al. 2012, *Icarus*, 220, 958
- Peralta, J., Lee, Y. J., Hueso, R., et al. 2017b, *Geophysical Research Letters*, 44, 3907, 2017GL072900.
<http://dx.doi.org/10.1002/2017GL072900>
- Peralta, J., Hueso, R., Sánchez-Lavega, A., et al. 2017c, *Nature Astronomy*, 1, 0187
- Piccioni, G., Drossart, P., Suetta, E., et al., eds. 2007, *ESA Special Publication*, Vol. 1295, *VIRTIS: The Visible and Infrared Thermal Imaging Spectrometer*
- Rayner, J. T., Toomey, D. W., Onaka, P. M., et al. 2003, *The Publications of the Astronomical Society of the Pacific*, 115, 362
- Reddy, B. S., & Chatterji, B. N. 1996, *IEEE Transactions on Image Processing*, 5, 1266
- Rossow, W. B., del Genio, A. D., & Eichler, T. 1990, *Journal of Atmospheric Sciences*, 47, 2053
- Samritjarapon, O., & Chitsobhuk, O. 2008, in 2008 *International Symposium on Communications and Information Technologies*, 364–367
- Sánchez-Lavega, A., Lebonnois, S., Imamura, T., Read, P., & Luz, D. 2017, *Space Science Reviews*, 212, 1541
- Sánchez-Lavega, A., Hueso, R., Piccioni, G., et al. 2008, *Geophysical Research Letters*, 35, 13204
- Satoh, T., Nakamura, M., Ueno, M., et al. 2016, *Earth, Planets, and Space*, 68, 74
- Satoh, T., Sato, T. M., Nakamura, M., et al. 2017, *Earth, Planets, and Space*, 69, 154
- Schubert, G. 1983, *General circulation and the dynamical state of the Venus atmosphere*, ed. D. M. Hunten, L. Colin, T. M. Donahue, & V. I. Moroz (University of Arizona Press), 681–765
- Takagi, M., Sugimoto, N., Ando, H., & Matsuda, Y. 2018, *Journal of Geophysical Research (Planets)*, 123, 335
- Takagi, S., & Iwagami, N. 2011, *Earth, Planets, and Space*, 63, 435
- Tavenner, T., Young, E. F., Bullock, M. A., Murphy, J., & Coyote, S. 2008, *Planetary and Space Science*, 56, 1435
- Titov, D. V., Svedhem, H., Koschny, D., et al. 2006, *Planetary and Space Science*, 54, 1279